RSC Advances

PAPER

View Article Online
View Journal | View Issue

Cite this: *RSC Adv.*, 2023, **13**, 28112

Fluorapatite nanorod arrays with enamel-like bundle structure regulated by iron ions

Yidi Li, *[ab] Hang Ping,[bc] Quanmin Xie,[a] G. Yang,[a] Jianguo Xu,[d] Mingming Zhong[c] and Kun Wang *[e]

Pigmented rodent tooth enamel is mainly composed of parallel hydroxyapatite nanorods and a small amount of organic matrix. These hydroxyapatite nanorods tend to be carbonated and contain traces of iron, fluorine, and magnesium. The pigmented rodent tooth enamel which contains trace iron is stronger and more resistant to acid corrosion than unpigmented rodent enamel, which could provide inspiration for the preparation and synthesis of high performance and corrosion resistant artificial materials. However, the regulatory role and mechanical enhancement of iron ions in enamel growth are unclear. Here, we synthesized enamel-like fluorapatite nanorod arrays *in vitro* using a mineralization technique at room-temperature. To investigate the regulatory effect of iron ions on the fluorapatite nanorod arrays (FAP-Fe), the phosphate solution is slowly transfused dropwise in the calcium ion solution, and different concentrations of iron ions are added to the calcium ion solution in advance. We demonstrated that fluorapatite nanorod arrays (FAP) can be epitaxially grown from amorphous calcium phosphate nanoparticles and iron ions can improve the microstructure of FAP nanorod arrays and obtain the same enamel bundle structure as the natural enamel. Moreover, high concentration of iron ions can inhibit the crystallization of fluorapatite. The FAP-Fe nanorod arrays controlled by 0.02 mM Fe^{3+} have good mechanical properties. Their hardness is 1.34 ± 0.02 GPa and Young's modulus is 65.3 ± 0.4 GPa, respectively. This work is helpful to understand the role of trace elements in natural enamel in the regulation of enamel formation and to provide a theoretical foundation for the preparation of high strength artificial composites, which can play a greater role in the fields of biological alternative materials, anti-oil coating, oil/water separation, anti-bioadhesion and so on.

Received 31st May 2023
Accepted 17th September 2023

DOI: 10.1039/d3ra03652a

rsc.li/rsc-advances

1. Introduction

Nature is a master of designing and synthesizing materials, giving us many inspirations for artificial materials design and synthesis.[1–7] Natural biological materials are usually synthesized by organisms through simple inorganic minerals and organic materials at room temperature and exhibit special properties, such as dental enamel[8–10] and nacre.[11–13] Dental enamel is located in the outermost layer of a tooth, approximately 2 mm, which can protect the inner layer of dentin from destruction.[14] Tooth enamel can withstand up to 2000 bites a day without being destroyed, and can adapt to the acidic environment in the mouth cavity.[15] It is thanks to the complex structure and composition of tooth enamel.[16–18] Dental enamel consists of interlocking prisms, which are formed by hydroxyapatite ($Ca_5(PO_4)_3OH$, HAP) nanorods doped with trace elements such as iron, magnesium and fluorine. These nanorods are highly assembled into bundles and exhibit high toughness.[19–21]

Researchers developed various methods to mimic the columnar structure of tooth enamel to achieve similar excellent properties.[8,22–25] Yeom *et al.* adopted a hydrothermal method to grow columnar ZnO on a polymeric matrix.[8] The static and dynamic mechanical properties of the enamel-like ZnO nanocomposite were similar to those of natural human enamel. Wei *et al.* adopted a microscale additive manufacturing method to synthesis an enamel-like structure materials consisted of TiO_2 nanorods and polymers.[22] The synthetic composites showed a Young's modulus and hardness of 81 and 1.56 GPa, respectively.

Recently, researchers found that trace elements, such as iron, magnesium in tooth enamel can tremendously improve their mechanical properties.[16,18,26,27] Cairney *et al.* use atom probe tomography to confirm that in human tooth enamel, the most magnesium ions are confined in the amorphous calcium phosphate between hydroxyapatite nanorods to form a Mg-rich intergranular phase.[16] Joester *et al.* also found the enrichment of Mg, F, Na and other trace elements in the amorphous

[a]State Key Laboratory of Precision Blasting, Jianghan University, Wuhan, 430056, P. R. China. E-mail: ydli@jhun.edu.cn
[b]Hubei Longzhong Laboratory, Xiangyang, 441000, Hubei, P. R. China
[c]State Key Laboratory of Advanced Technology for Materials Synthesis and Processing, Wuhan University of Technology, Wuhan, 430070, P. R. China
[d]Ordnance NCO Academy Army Engineering University, Wuhan, 430070, P. R. China
[e]State Key Laboratory of Silicate Materials for Architectures, Wuhan University of Technology, Wuhan, 430070, P. R. China

intergranular phase of human tooth enamel, and proved that the chemical gradient in tooth enamel is the cause of residual stress which improve the mechanical resilience of enamel.[18] Moreover, the trace iron in pigmented rodent tooth enamel renders it both stronger and more resistant to acid corrosion than unpigmented rodent enamel.[15] These results indicate that the presence of trace elements of iron and magnesium in enamel has an significant role in the process of growth and mechanical properties of tooth enamel. Many researchers have studied the crystallization behavior of inorganic ions such as magnesium ions on calcium carbonate and calcium phosphate.[28,29] It is found that magnesium ion can regulate the crystal growth of calcium carbonate and calcium phosphate. For example, magnesium ion can regulate the crystal type of calcium carbonate. However, only a small portion of research has focused on the regulatory role and mechanical enhancement of this trace elements in artificial composite materials. Fu *et al.* introduced magnesium ion regulation *in vitro* synthesis of fluorapatite nanorod arrays of dental enamel composites.[10] It is found that the grain size of fluorapatite nanorods can be effectively controlled by magnesium ion regulation and the array of fluorapatite nanorods can be arranged more closely. But the regulatory role of iron ions in enamel-like materials is still unclear.

This work, we adopted a two-step mineralization technique to synthesize an enamel-like fluorapatite nanorod arrays regulated by Fe^{3+} (FAP-Fe) *in vitro* at environment temperature. Firstly, a base layer consisting of amorphous calcium phosphate was prepared under the control of high concentrations of magnesium ions. Subsequently, the FAP-Fe nanorod arrays was epitaxially grown on the base layer with the regulation of Fe^{3+}. Fe^{3+} can improve the microstructure of FAP array and obtain the same enamel bundle structure as the natural enamel. Moreover, high concentration of Fe^{3+} can inhibit the crystallization of fluorapatite. The hardness (1.34 ± 0.02 GPa) and Young's modulus (65.3 ± 0.4 GPa) of the synthetic FAP-Fe nanorod arrays are close to those of natural rodent tooth enamel. The hardness and Young's modulus of the synthetic fluorapatite nanorod arrays without iron ions control (FAP) are 0.64 ± 0.05 GPa and 39.4 ± 1.5 GPa, respectively. This finding is helpful to understand the role of trace elements in natural enamel in the regulation of enamel formation and mechanical properties and also provide a theoretical foundation for the preparation of high strength artificial composites.

2. Experimental

2.1. Materials

Polyacrylic acid (PAA, Mn = 100 kg mol^{-1}), polyvinylpyrrolidone (PVP, Mn = 60 kg mol^{-1}), $CaCl_2 \cdot 2H_2O$ ($M_W = 147$), Na_2CO_3 ($M_W = 105.9$), $Na_2HPO_4 \cdot 12H_2O$ ($M_W = 358.14$), NaF ($M_W = 147$), $MgCl_2 \cdot 6H_2O$ ($M_W = 203.3$), $FeCl_2 \cdot 6H_2O$ ($M_W = 162.2$) were purchased from Sigma-Aldrich.

2.2. Deposition of organic films

First, the stain on the surface of the glass sheet is cleaned. Second, a 3 mg mL^{-1} PVP solution was spin-coating on the cleaned glass sheet at 3000 rpm for 20 s to obtain a continuous PVP film. Then, a 3 mg mL^{-1} PAA solution was continuous spin-coating on the glass sheet to obtain a PAA film. The organic film of $(PVP/PAA)_5$ was obtained by rotating coating 10 times alternately. The glass sheet coated with an organic film is then dipped into a sodium hydroxide solution (pH = 12) for 20 min, removed and washed, and crosslinked with UV light for 10 min. The multi-layer PAA/PVP film will partially dissolve in the sodium hydroxide solution, forming holes. At this time, the carboxyl group contained in the PAA will attract the calcium ions in the mineralization solution to nucleate and crystallize on the surface of the film, forming a firmly bonded amorphous calcium phosphate transition layer.

2.3. Growth of amorphous calcium phosphate transition layer

The amorphous calcium phosphate transition layer was obtained *via* mineralization with the present of high concentration of Mg^{2+}. A 50 mL solution of 2.7 mM $Na_2HPO_4 \cdot 12H_2O$ and 2.7 mM NaF was added to a beaker of a 50 mL solution with 5.4 mM $CaCl_2 \cdot 2H_2O$ and 3 mM $MgCl_2 \cdot 6H_2O$ at a flow rate of 1 mL h^{-1} through a peristaltic pump. The glass sheet coated with an organic film was placed at bottom of beaker to growth amorphous calcium phosphate transition layer. The whole experiment lasted for 50 hours, and the experimental temperature was controlled at 25 °C.

2.4. Overgrowth

A 50 mL solution of 2.7 mM $Na_2HPO_4 \cdot 12H_2O$ and 2.7 mM NaF was added to a beaker of a 50 mL solution with 5.4 mM $CaCl_2 \cdot 2H_2O$ and different concentrations of $FeCl_2 \cdot 6H_2O$ at a flow rate of 0.52 mL h^{-1} through a peristaltic pump. The glass sheet with transition layer was placed at the bottom of the beaker to growth the FAP nanorod arrays.

2.5. Cytotoxic activities text of FAP-Fe nanorod arrays

Osteoblasts (Procell Life Science & Technology, Wuhan) were cultured in Dulbecco's modified Eagle's medium (DMEM, Gibco, USA), 10% fetal bovine serum (FBS, Gibco, USA), 1% penicillin-streptomycin (PS, Sigma, USA) and 1% L-glutamine (Gibco, USA) in a humidified incubator at 37 °C with a 5% carbon dioxide atmosphere. The sample with FAP-Fe array controlled by 0.02 mM Fe^{3+} on the glass plate was the experimental group, and the blank glass plate was the control group. Three parallel samples were used in the Cytotoxic activities test. The glass plates for test were sterilized under ultraviolet radiation for 1 h in a biosafety cabinet (BioX Scientific, USA) and then were placed at the bottom of a 24-well plate. The cell density of the osteoblasts was adjusted to 3×10^4 and the cell suspension was injected into a 24-well plate, which contained the glass plate. Fresh culture medium was supplemented in the 24-well plate after 4 h.

The glass plate with FAP-Fe nanorod arrays controlled by 0.02 mM Fe^{3+} and blank glass plate were seeded with osteoblasts and cultured for 7 days. An equivalent volume of culture medium was sucked out and discarded before the cell counting

kit-8 (CCK-8, Sangon Biotech, China) solution was injected into the 24-well plate and incubated for 2 h at 37 °C. The culture medium after incubation was transferred to a 96-well plate for absorbance detection at 450 nm using a microplate spectrophotometer (BioTek Instruments, USA). For statistics analysis, all data were from triplicate measurements and are reported as the mean and standard deviation.

2.6. Characterization

Crystal structures were characterized *via* a XRD (Bruker, Germany) with Cu Kα radiation ($\lambda = 1.54$ Å). The morphological of the transition layer and overlayer were observed *via* a field-emission SEM (FESEM; SU-8020, Hitachi, Japan) at an accelerating voltage of 5 kV. For TEM analysis, samples were dispersed in an alcohol solution and then the copper mesh was dipped into the alcohol solution several times before being observed. The Raman spectroscopy (Renishaw plc, Wottonunder-Edge, U.K.) was tested at 200–1500 cm^{-1} equipped with a 633 nm laser. The FTIR spectrometry (Nicolet Nexus (an intelligent spectrometer), Thermo Fisher Scientific, Massachusetts) was tested at 4000–400 cm^{-1}. The underwater contact angle was tested using a DSA100 contact angle/interface system (Data-Physics). Three different regions were tested at the same time to find the average value. The mechanical properties of the FAP-Fe nanorod arrays and FAP nanorod arrays simples were tested using a nanoindentation tests (G200, Keysight Technologies, Santa Rosa, CA).

3. Results and discussion

3.1. Mineralization of fluorapatite nanorod arrays regulated by Fe^{3+}

To prepare FAP-Fe nanorod arrays regulated by Fe^{3+} at room temperature, a two-step mineralization method was adopted (Fig. 1a). First, a uniform polymeric film was obtained on a hydrophilic glass sheet by spin-coating methods. The glass sheet was then placed into a mineralizing solution with 1.5 mM concentration of Mg^{2+}. After mineralization for 48 h, a transition layer consisted of spherical particles with the diameter about 200 nm (Fig. 1b). Second, the glass sheet was continue placed at the bottom of the beaker containing a new mineralizing solution with a low concentration of Fe^{3+}. After mineralization for 96 h, an FAP-Fe nanorod arrays with an enamel-like bundle structure was epitaxial growth on the base layer. Fig. 1c shows a SEM image of cross-sectional structure of a FAP-Fe nanorod arrays. The FAP-Fe nanorod arrays was consisted of a highly aligned nanorods about 250 nm in diameter. The thickness of FAP-Fe array is about 2.5 μm. The top-view SEM images (Fig. 1d) showed that each nanorod is made of finer nanowires with the diameter of 80 nm, similar to the enamel bundles found in natural tooth enamel. Natural tooth enamel is made of interwoven enamel bundles assembled from hydroxyapatite nanorods and the hierarchy of enamel bundles in tooth enamel is more complex and sophisticated. The TEM images and EDS mapping images of transition layer were showed in Fig. 2. The diffusion ring in selective electron diffraction result indicates that the nanoparticles of transition layer are amorphous. Nanoparticles of transition layer contains elements of Ca, Mg, O, F, P.

3.2. Regulation effect of Fe^{3+} concentration on the FAP-Fe nanorod arrays

The regulation effect of Fe^{3+} concentration on the FAP-Fe nanorod arrays was studied. With the regulatory of 0.02 mM Fe^{3+}, dozens of fluorapatite nanowire are tightly tied together to form rods about 250 nanometers in diameter, which are highly ordered and grow vertically after mineralization of 96 h (Fig. 3a). In the X-ray diffraction (XRD) pattern (Fig. 3g), the intensities of diffraction peaks at 25.84° and 53.18° corresponding to crystal planes 002 and 004 are significantly higher than that of the

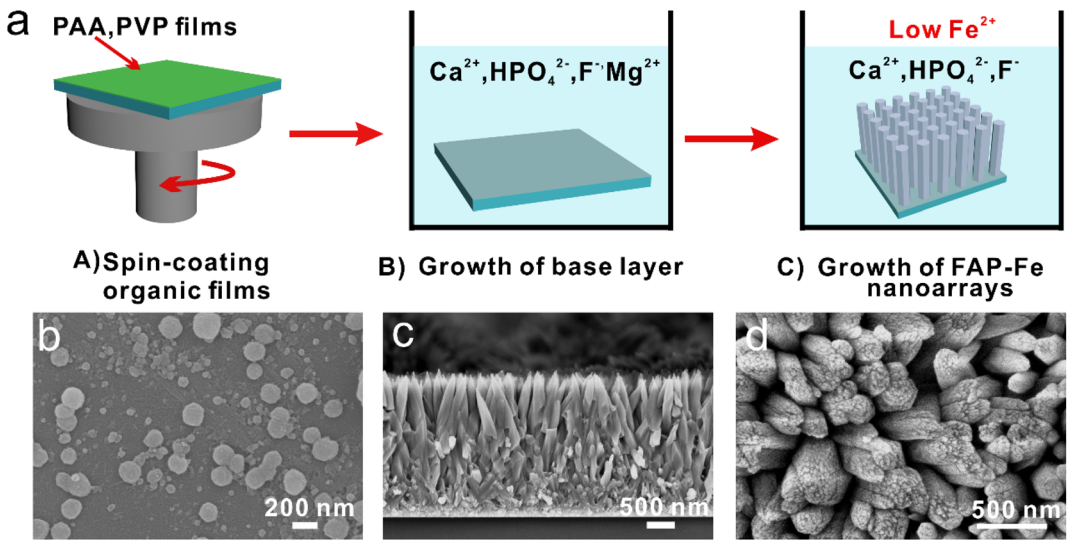

Fig. 1 (a) Schematic diagram of the fabrication process of FAP-Fe nanoarrays regulated by Fe^{3+}. (b) SEM image of spherical particles in base layer. (c and d) Cross sectional and top-view SEM images of FAP-Fe nanoarrays controlled by 0.02 mM Fe^{3+}.

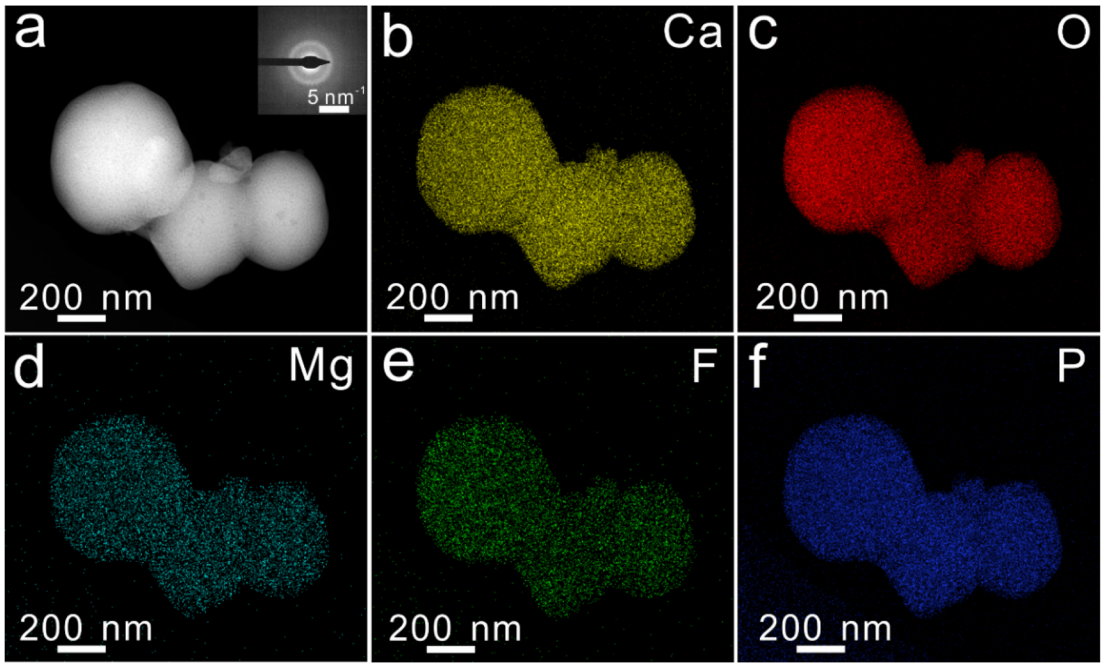

Fig. 2 TEM-EDS mapping of spherical particles in base layer.

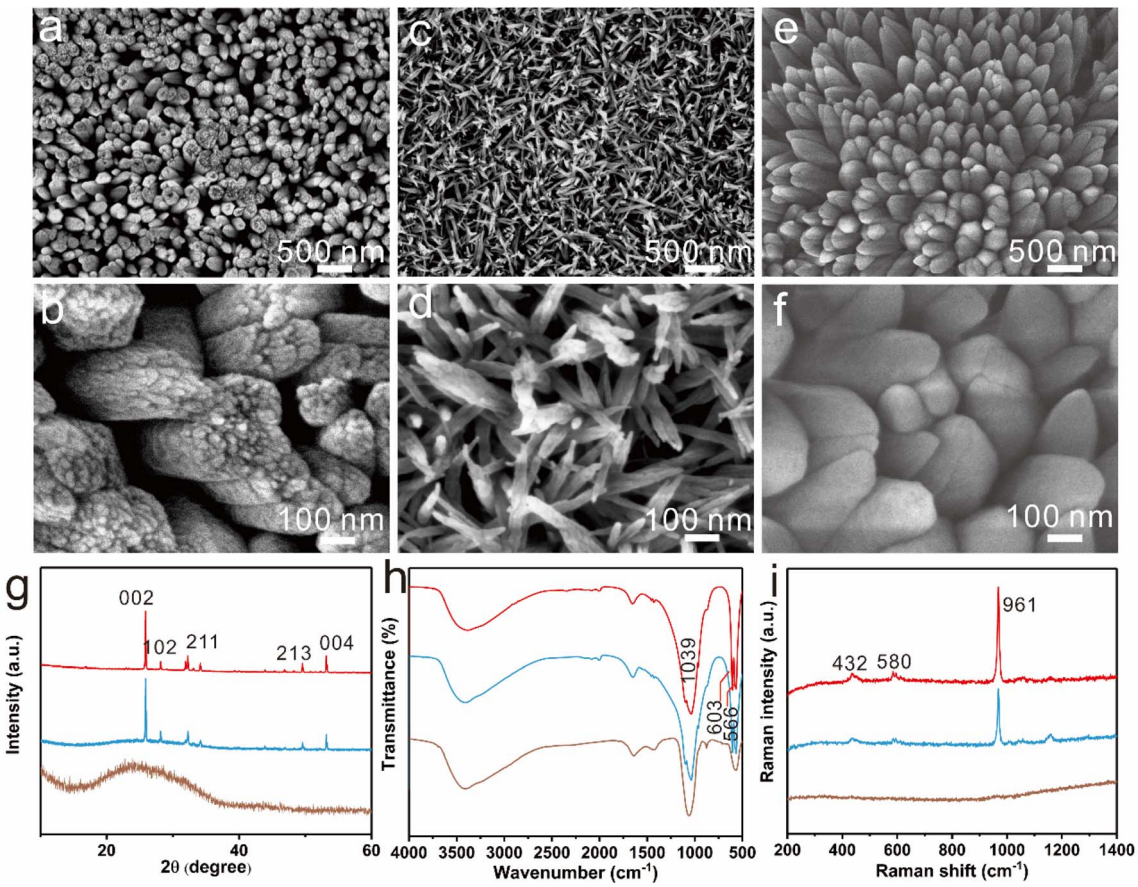

Fig. 3 Top-view SEM images of (a and b) FAP-Fe (0.02 mM), (c and d) FAP-Fe (0.2 mM), (e and f) FAP. (g) XRD patterns, (h) FTIR spectrum, and (i) Raman spectrum of FAP-Fe (0.02 mM) (red line), FAP-Fe (0.2 mM) (brown line) and FAP arrays (blue line).

other crystal planes, indicating that the nanorods are all vertically aligned. Increase the regulatory concentration of Fe^{3+}, the nanorods get thinner, only about 50 nanometers in diameter, and the nanorods are disordered with the regulatory of 0.2 mM Fe^{3+} (Fig. 3c and d). X-ray diffraction (XRD) pattern (Fig. 3g) confirmed the amorphous nature. This indicates that high concentration of iron ions can inhibit the crystallization of fluorapatite. As a control specimen, FAP arrays were also prepared without regulation of Fe^{3+} (Fig. 3e and f). The FAP arrays are consisted of nanorods about 200 nm in diameter. The FAP nanorods are tightly packed and its surface is smooth. XRD pattern also indicates that the FAP nanorods are all vertically aligned. The Fourier transform infrared (FTIR) spectra patterns of FAP, FAP-Fe (0.02 mM) and FAP-Fe (0.2 mM) are showed in Fig. 3h. The bands at 566 and 602 cm^{-1} belonged to the ν4 bending modes of PO_4^{3-};[30] and the band at 1039 cm^{-1} belonged to the ν3 bending mode.[31] The FAP-Fe (0.2 mM) showed an unsplit peak which indicating it is amorphous. It indicates that high concentration of Iron ions can inhibit the crystallization of fluorapatite. The Raman spectra of FAP, FAP-Fe (0.02 mM) and FAP-Fe (0.2 mM) are showed in Fig. 3i. The high intensity Raman spectral peak at 961 cm^{-1} represents the highly ordered (FAP) and FAP-Fe (0.02 mM) crystalline arrays. Moreover, the Raman spectral peak of the FAP-Fe (0.02 mM) shifted slightly to the left compared with FAP-Fe by 1.12 cm^{-1}. It may because that some iron ions replace the position of calcium ions, and the atomic radius of iron ions is larger than that of calcium ions, which will expand the fluorapatite lattice and reduce the Raman vibration frequency. The Raman spectral peaks of FAP-Fe (0.2 mM) disappeared because it was amorphous. The EDS mapping images (Fig. 4) indicated the nanorod of FAP-Fe arrays contains elements of Ca, Fe, O, F, P. This proves that iron ions successfully enter the fluorapatite nanorods.

3.3. Growth process of the FAP-Fe nanorod arrays

We further studied the growth process of the FAP-Fe (0.02 mM) and FAP nanorod arrays during the mineralization. After mineralization for 12 h, many small nanorods grow epitaxial from the spherical particles of base layer with regulation of 0.02 mM Fe^{3+} (Fig. 5a). This nanorods are disordered. With the progress of mineralization, more and more nanorods grow, and the order degree of nanorods increases, and the diameter of nanorods becomes larger (Fig. 5b). After mineralization for 72 h, the thickness of the FAP-Fe and the order degree of the nanorods increase greatly. The diameter of FAP-Fe arrays is about 300 nm and the thickness is about 3 μm (Fig. 5c). There is a similar growth process in FAP nanorods (Fig. 5d–f). The growth process of FAP arrays is faster and the order degree of nanorods is lower than that of FAP-Fe arrays.

3.4. Under-water superoleophobicity

Fish scales and shells keep their surfaces clean for a long time because of the nanostructures on their surfaces that are hydrophilic and under-water superoleophobicity.[32] The synthesized fluorapatite arrays show similar underwater super hydrophobicity. We tested the contact angle (CA) of FAP-Fe arrays and FAP arrays (Fig. 6). The FAP-Fe arrays and FAP arrays exhibited excellent hydrophilic with a CA of 8.8 ± 0.5° and 2.4 ± 0.3° respectively. The CA of underwater oil on the FAP-Fe and FAP nanorod arrays were also characterized, which are 148° ± 1.4° and 154° ± 2.5° respectively. The micro-/nano-texture of FAP-Fe and FAP nanorod arrays showed hydrophilic properties, which can capture water molecules on its surface, reducing oil contamination.[33,34] Because of the lack of Fe^{3+} regulation, FAP nanorod arrays are rough and their underwater CA is bigger, so they exhibit underwater superhydrophobic

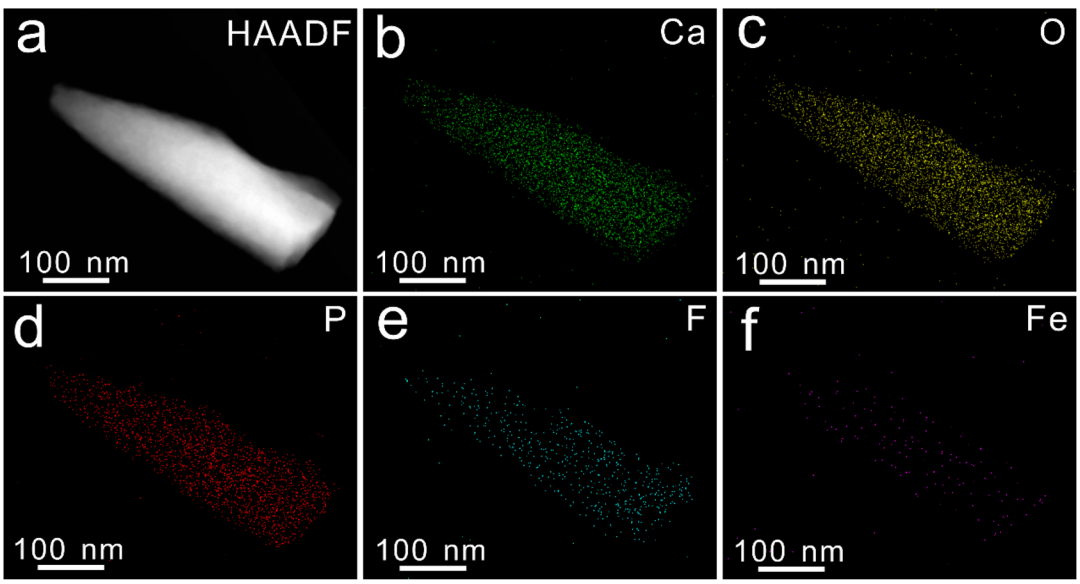

Fig. 4 TEM-EDS mapping of a single FAP-Fe nanorod (0.02 mM).

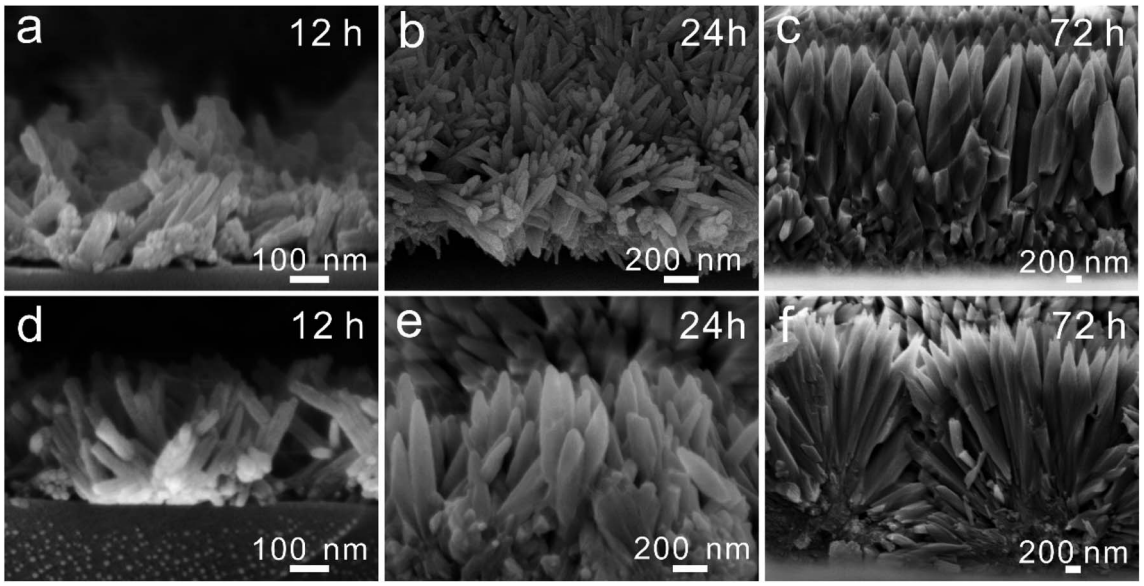

Fig. 5 (a–c) SEM images exhibited the growth of FAP-Fe arrays (12, 24 and 72 h). (d–f) SEM images exhibited the growth of the FAP arrays (12, 24 and 72 h).

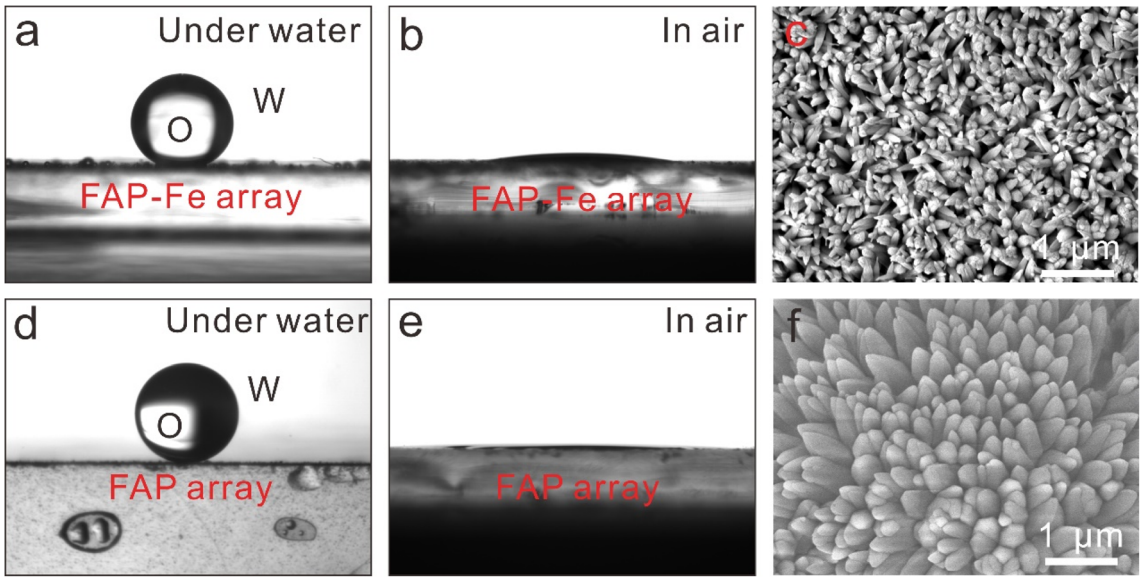

Fig. 6 (a and b) Pictures showing the contact angle test of FAP-Fe (0.02 mM) nanorod arrays. (c) Top-view SEM image of FAP-Fe (0.02 mM) arrays. (d and e) Pictures showing the contact angle test of FAP arrays. (f) SEM image of FAP nanorod arrays.

properties, which has important potential applications in anti-oil coating, oil/water separation and anti-bioadhesion.

3.5. Mechanical properties

The hardness (H) and Young's modulus (E_Y) of the FAP-Fe (0.02 mM) nanorod arrays and FAP nanorod arrays were tested by means of a nanoindentation measurements. The synthetic FAP-Fe arrays exhibit H and E_Y values of 1.34 ± 0.02 GPa and 65.3 ± 0.4 GPa, respectively (Fig. 7a and b). These properties should be attributed to the closely packed nanorods forming a highly ordered nanorod arrays controlled by Fe^{3+}. As a comparison, the H and E_Y of synthetic FAP nanorod arrays are 0.64 ± 0.05 and 39.4 ± 1.5 GPa, respectively. This difference in mechanical properties is mainly due to the order degree of nanorods in FAP array is not high, and the gap between nanorods is large, which seriously affects the mechanical properties. Load-displacement curves is exhibited in Fig. 7c.

3.6. Biocompatibility

The biological activity of the FAP-Fe nanorod arrays controlled by 0.02 mM Fe^{3+} was tested by incubating them in the cell culture medium. The proliferation of osteoblasts seeded on the

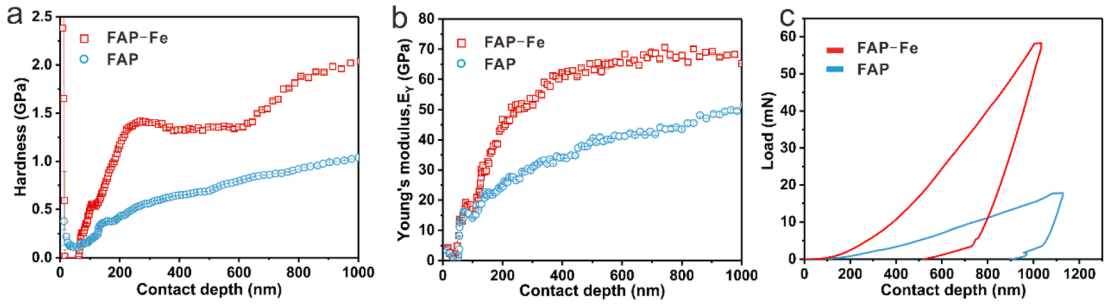

Fig. 7 (a) Young's modulus–displacement curves. (b) Hardness-displacement curves. (c) Load-displacement curves.

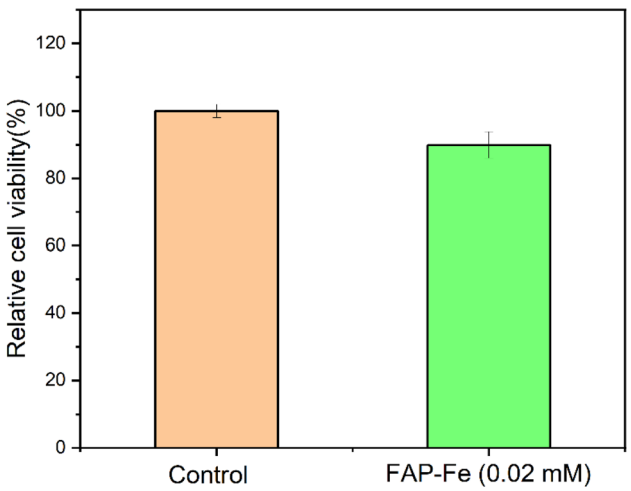

Fig. 8 Cytotoxicity test on FAP-Fe nanorod arrays (0.02 mM).

FAP-Fe (0.02 mM) was assessed using a CCK-8 kit. It was observed that the survival rate of osteoblasts on the array was close to 90% after 7 days of culture (Fig. 8). This preliminarily indicates that the FAP-Fe nanorod arrays has good biocompatibility and has the great potential as a dental repair material.

4. Conclusions

In this study, an enamel-like bundle structure fluorapatite array regulated by Fe^{3+} (FAP-Fe) was synthesized *in vitro* at environment temperature. Fe^{3+} can improve the microstructure of FAP array and obtain the same enamel bundle structure as the natural enamel. Moreover, high concentration of Fe^{3+} can inhibit the crystallization of fluorapatite. The FAP-Fe nanorod arrays controlled by 0.02 mM Fe^{3+} has good mechanical properties. Its hardness is 1.34 ± 0.02 GPa and Young's modulus is 65.3 ± 0.4 GPa, respectively. This finding is helpful to figure out the role of trace elements in the regulation of enamel formation and mechanical properties and also provide a theoretical foundation for the preparation of high strength artificial composites. Due to the limitations of the mechanism and synthesis methods, we hope to further study the role of iron ion in the regulation of biomineralization. It will inspire us to prepare macro-sized biomimetic composites with excellent properties, which can play a greater role in the fields of biological alternative materials, anti-oil coating, oil/water separation and anti-bioadhesion and so on.

Author contributions

YD Li conducted the experiments and wrote the paper. K Wang and H Ping supervised the project. QM Xie, H Ping and G. Yang guided the theoretical analysis part. JG Xu and MM Zhong revised the paper. All authors contributed to the general discussion.

Conflicts of interest

The authors declare no conflict of interest

Acknowledgements

The authors would like to thank Miss Ting-ting Luo (Center for Materials Research and Analysis, Wuhan University of Technology) for her help in the TEM analysis. The project was supported by the National Natural Science Foundation of China (52302095), Open Fund of Hubei Longzhong Laboratory (2022KF-04), Jianghan University Doctoral Research Initiation Fund Project (PBSKL-2023-QD-05), Key research and development project of Hubei Province (2020BCA084, 2021BAD004).

References

1 J. Xie, H. Ping, T. Tan, L. Lei, H. Xie, X. Y. Yang and Z. Fu, *Prog. Mater. Sci.*, 2019, **105**, 100571.
2 L. A. Estroff, *Chem. Rev.*, 2008, **108**, 4329–4331.
3 M. A. Meyers, P.-Y. Chen, A. Y.-M. Lin and Y. Seki, *Prog. Mater. Sci.*, 2008, **53**, 1–206.
4 L. Ren, Z. Wang, L. Ren, Z. Han, Q. Liu and Z. Song, *Composites, Part B*, 2022, 110086.
5 Z. Liu, Z. Zhang and R. O. Ritchie, *Adv. Funct. Mater.*, 2020, **30**, 1908121.
6 F. Wang, X. Liao, H. Wang, Y. Zhao, J. Mao and D. G. Truhlar, *Interdisciplinary Materials*, 2022, **1**, 517–525.
7 J. Wei, C. Zhu, Z. Zeng, F. Pan, F. Wan, L. Lei, G. Nyström and Z. Fu, *Interdisciplinary Materials*, 2022, **1**, 495–506.
8 B. Yeom, T. Sain, N. Lacevic, D. Bukharina, S.-H. Cha, A. M. Waas, E. M. Arruda and N. A. Kotov, *Nature*, 2017, **543**, 95–98.

9 Y. Li, H. Ping, J. Wei, Z. Zou, P. Zhang, J. Xie, Y. Jia, H. Xie, W. Wang and K. Wang, *ACS Appl. Mater. Interfaces*, 2021, **13**, 25260–25269.
10 Y. Li, Y. Kong, B. Xue, J. Dai, G. Sha, H. Ping, L. Lei, W. Wang, K. Wang and Z. Fu, *ACS Nano*, 2022, **16**, 10422–10430.
11 H. D. Espinosa, J. E. Rim, F. Barthelat and M. J. Buehler, *Prog. Mater. Sci.*, 2009, **54**, 1059–1100.
12 L. B. Mao, H. L. Gao, H. B. Yao, L. Liu, H. Cölfen, G. Liu, S. M. Chen, S. K. Li, Y. X. Yan and Y. Y. Liu, *Science*, 2016, **354**, 107–110.
13 X. Zhang, K. Wu, Y. Ni and L. He, *Nat. Commun.*, 2022, **13**, 7719.
14 L. H. He and M. V. Swain, *J. Mech. Behav. Biomed. Mater.*, 2008, **1**, 18–29.
15 L. M. Gordon, M. J. Cohen, K. W. MacRenaris, J. D. Pasteris, T. Seda and D. Joester, *Science*, 2015, **347**, 746–750.
16 A. La Fontaine, A. Zavgorodniy, H. Liu, R. Zheng, M. Swain and J. Cairney, *Sci. Adv.*, 2016, **2**, e1601145.
17 L. M. Gordon and D. Joester, *Front. Physiol.*, 2015, **6**, 57.
18 K. A. DeRocher, P. J. Smeets, B. H. Goodge, M. J. Zachman, P. V. Balachandran, L. Stegbauer, M. J. Cohen, L. M. Gordon, J. M. Rondinelli and L. F. Kourkoutis, *Nature*, 2020, **583**, 66–71.
19 A. Meckel, W. Griebstein and R. Neal, *Arch. Oral Biol.*, 1965, **10**, 775–783.
20 J. Eastoe, *Nature*, 1960, **187**, 411–412.
21 B. Kerebel, G. Daculsi and L. Kerebel, *J. Dent. Res.*, 1979, **58**, 844–851.
22 J. Wei, H. Ping, J. Xie, Z. Zou, K. Wang, H. Xie, W. Wang, L. Lei and Z. Fu, *Adv. Funct. Mater.*, 2020, **30**, 1904880.
23 H. Zhao, S. Liu, Y. Wei, Y. Yue, M. Gao, Y. Li, X. Zeng, X. Deng, N. A. Kotov and L. Guo, *Science*, 2022, **375**, 551–556.
24 Z. Chen, Z. Miao, P. Zhang, H. Xiao, H. Liu, C. Ding, H. Tan and J. Li, *J. Mater. Chem. B*, 2019, **7**, 5237–5244.
25 K. Onuma and M. Iijima, *Sci. Rep.*, 2017, **7**, 1–10.
26 J. Tao, D. Zhou, Z. Zhang, X. Xu and R. Tang, *Proc. Natl. Acad. Sci. U. S. A.*, 2009, **106**, 22096–22101.
27 N. Blumenthal, F. Betts and A. Posner, *Calcif. Tissue Res.*, 1977, **23**, 245–250.
28 Y. Nishino, Y. Oaki and H. Imai, *Cryst. Growth Des.*, 2009, **9**, 223–226.
29 B. Cantaert, A. Verch and Y. Y. Kim, *Chem. Mater.*, 2013, **25**, 4994–5003.
30 K. Tank, P. Sharma, D. Kanchan and M. Joshi, *Cryst. Res. Technol.*, 2011, **46**, 1309–1316.
31 L. Berzina-Cimdina and N. Borodajenko, *Infrared Spectrosc.: Mater. Sci., Eng. Technol.*, 2012, **12**, 251–263.
32 M. Liu, S. Wang, Z. Wei, Y. Song and L. Jiang, *Adv. Mater.*, 2009, **21**, 665–669.
33 T. Guo, L. Heng, M. Wang, J. Wang and L. Jiang, *Adv. Mater.*, 2016, **28**, 8505–8510.
34 X. Liu, J. Zhou, Z. Xue, J. Gao, J. Meng, S. Wang and L. Jiang, *Adv. Mater.*, 2012, **24**, 3401–3405.